Passivation Dynamics in the Anisotropic Deposition and Stripping of Bulk Magnesium Electrodes During Electrochemical Cycling

David J. Wetzel^a, Marvin A. Malone^a, Richard T. Haasch^b, Yifei Meng ^{b,c}, Henning Vieker ^d, Armin Golzhauser^d, Jian-Min Zuo^{b,c}, Nathan T. Hahn^e, Kevin R. Zavadil^e, Andrew A. Gewirth^a, and Ralph G. Nuzzo^a

^aDepartment of Chemistry, University of Illinois, Urbana, Illinois 61801, United States

^bFrederick Seitz Materials Research Laboratory, University of Illinois, Urbana, Illinois 61801, United States

^cDepartment of Materials Science and Engineering, University of Illinois, Urbana, IL 61801, United States

^dFakultät für Physik, Universität Bielefeld, Universitätsstr.25, D-33615 Bielefeld, Germany

^eSandia National Laboratories, PO Box 5800, Albuquerque, New Mexico, 87185, United States

Abstract

Although rechargeable magnesium (Mg) batteries show promise for use as a next generation technology for high density energy storage, little is known about the Mg anode solid electrolyte interphase and its implications for the performance and durability of a Mg-based battery. We explore in this report passivation effects engendered during the electrochemical cycling of a bulk Mg anode, characterizing their influences during metal deposition and dissolution in a simple, non-aqueous, Grignard electrolyte solution (ethylmagnesium bromide, EtMgBr, in tetrahydrofuran). Scanning electron microscopy images of Mg foil working electrodes after electrochemical polarization to dissolution potentials show the formation of corrosion pits. The pit densities so evidenced are markedly potential dependent. When the Mg working electrode is cycled both potentiostatically and galvanostatically in EtMgBr these pits, formed due to passive layer breakdown, act as the foci for subsequent electrochemical activity. Detailed microscopy, diffraction, and spectroscopic data show that further passivation and corrosion results in the anisotropic stripping of the Mg {0001} plane, leaving thin oxide-comprising passivated side wall structures that demark the {0001} fiber texture of the etched Mg grains. Upon long term cycling, oxide side walls formed due to the pronounced crystallographic anisotropy of the anodic stripping processes, leading to complex overlay anisotropic, columnar structures, exceeding 50 μm in height. The passive responses mediating the growth of these structures appear to be an intrinsic feature of the electrochemical growth and dissolution of Mg using this electrolyte.

Keywords:

Rechargeable magnesium battery Magnesium anode Passivation Corrosion Columnar growth

1. Introduction

Recently there has been an aggressive push toward the development of rechargeable batteries that use bulk metal anodes [1-7]. The use of metal anodes in energy storage devices is seen as advantageous due in part to their high theoretical energy densities and capacities.

Various performance related issues, however, have limited the development of market-ready, bulk metal anode-based rechargeable batteries. Lithium (Li) metal, for instance, has received significant attention in research, but to date viable technologies have yet to emerge due to battery failures that occur from the formation of Li dendrites that grow out from the metal anode surface as a result of repetitive charging and discharging [8]. Research into the causes and strategies for the elimination of Li metal dendrites is a subject of ongoing work in the field [9-13].

Due to its physical and chemical properties, magnesium (Mg) has been considered as an alternative anode to Li metal, especially for the case of rechargeable batteries for electric vehicles. Compared to Li, Mg is multivalent (with a theoretical volumetric capacity of 3832 versus 2062 mAh cm⁻³), more abundant, less toxic and, most importantly, less susceptible to dendritic growth. Metallic Mg is highly reactive, however and is thus susceptible to passivation, which is problematic for its use as an electrode. When exposed to air, Mg forms a passivation layer consisting of atmospheric contaminants, most notably oxide and hydroxide, although with proper surface preparation this passivating film can be reduced or eliminated [14]. Nevertheless, even if the initial oxide layer is removed, Mg can still be passivated from species developed as a consequence of electrochemical activity. The current literature suggests the reactivity of the electrolyte solvent plays a central role to this end. Such features of the reactivity of Mg have limited the use of solvents to primarily ethers [15].

Such issues notwithstanding, there has been a marked increase in work focused on the study of Mg rechargeable batteries [16-28]. The majority of this work has been focused on the discovery and characterization of novel non-aqueous electrolytes with large electrochemical windows. Hardly any work related to Mg rechargeable batteries has examined the morphology of bulk Mg anodes as result from extended electrochemical processing in non-aqueous solutions, except to note that Mg tends to form strongly passivated surfaces using electrolyte mimics of traditional Li-ion batteries [14].

In this paper we examine the morphologies of Mg anodes after polarization to dissolution potentials, as well as cyclic potential steps, in order to develop insights into the passivation dynamics and electrochemically-mediated corrosion processes of Mg as occur in Grignard-based electrolytes and how these processes impact the viability of Mg as an energy storage material. We show that upon extensive cycling the inherent dynamics of the processes involved are distinguished by strong crystallographic anisotropies, and passive film formation particularly during Mg stripping, that lead to the growth of anisotropic columns of Mg that could lead to battery failures not unlike those that result from Li dendrites.

2. Experimental Details

Ethylmagnesium bromide, 1.0 M in tetrahydrofuran (EtMgBr), the electrolyte used for all electrochemical experiments, was purchased from Sigma-Aldrich and used with no further preparation. All electrochemical experiments were carried out in an Argon-filled MBRAUN LABstar glovebox. Electrochemical experiments were performed using either a CH Instrument 650 B or 660 D analyzer/workstation. Electrochemical cell components were acid washed, rinsed with Milli-Q water, and oven dried before each use. Magnesium foil (GalliumSource,

LLC), 99.95% and 0.05 mm thick, was used as the working electrode for most experiments. Immediately prior to each experiment a new piece of Mg foil was polished with 421 polishing compound, a felt pad, and rotary tool (all purchased from Dremel) inside the glovebox, then washed with THF and wiped with a cloth to remove excess polishing compound. Although several chemical polishing methods were attempted, mechanical polishing inside the glovebox resulted in the best finish and thinnest passivation layer on Mg (as confirmed by electrochemical and microscopy measurements). For all experiments the counter and reference electrodes used were similarly polished strips of Mg ribbon.

The scanning electron microscope (SEM), x-ray diffraction (XRD), x-ray photoelectron spectroscopy (XPS), and focused ion beam (FIB) instrumentation used in this work are located at the Frederick Seitz Materials Research Laboratory (FS-MRL) on the campus of the University of Illinois at Urbana-Champaign and described at mrl.illinois.edu. The helium ion microscope (HIM) images were taken at Bielefeld University in Bielefeld, Germany (see below).

A Hitachi S4700 high resolution SEM and a JEOL 7000F analytical SEM were used in the collection of SEM images. After the completion of each experiment, the Mg foil was rinsed with THF and allowed to dry inside the glovebox after which it was transferred to the SEM. During transfer to the SEM, the Mg foil is exposed to air therefore, in order to limit this exposure, Mg foils were transferred immediately before analysis.

A PANalytical Philips X'pert MRD system equipped with a Cu K- α source at 0.15418 nm was used for x-ray diffraction experiments. A polycrystalline Mg substrate was purchased from MTI Corporation and used as a reference. XRD 2-theta scans were taken at a scan rate of 2° min⁻¹ for both the Mg foil and polycrystalline substrate. Pole figures of the (002) diffraction

line were also obtained for both samples of Mg. XRD results were analyzed using JADE XRD analysis software.

A Physical Electronics PHI 5400 equipped with a Mg source and a pass energy of 35.75 eV, was used to obtain high resolution XPS results for polished, stripped, and cycled Mg foils. Electrochemical experiments were conducted inside the glovebox after which, the foils were rinsed with THF and then immediately placed within an XPS transfer vessel. The XPS vessel was then doubly sealed in resealable bags and transported directly from the glovebox to the XPS instrument, where the vessel works as a load lock. The transfer procedure was done to keep the samples from being exposed to air. The samples were electrically grounded, and binding energies were calibrated using the Ag 3d5/2 peak at 368.06 eV (+0.24 eV) measured from a reference foil within the vacuum chamber.

A FEI Helios 600i focused ion beam (FIB) with a gallium ion source was used to mill structures in preparation for helium ion microscope imaging. The HIM images were taken with a Carl Zeiss Orion Plus helium ion microscope operating with an accelerating voltage of about 39.5 kV and a current of about 0.4 pA. Sample distance was 11 mm with a spot size of 10 µm and each image used averaging of 32 lines with a dwell time of 1 µs per pixel.

3. Results and Discussion

Fig. 1a shows the current-time transients (solid traces) obtained from three Mg foil working electrodes stepped from open circuit potential (approximately 50 mV vs. Mg) to potentials held at 500, 700, and 900 mV in a 1.0 M solution of EtMgBr in THF for 1800 seconds. The potentiostatic stripping experiments highlight the initial state characteristics of the anode surface and maintain a surface at constant potential in order to evaluate the relative contribution

of thermodynamic and kinetic contributions to stripping. Current-time transients of the electrochemically-mediated metal dissolution have previously elucidated the relative kinetic and thermodynamic contributions for Cu in an aqueous system[29]. Souto et al. used nucleation and growth models to characterize the potentiostatically controlled dissolution of a Cu electrode and above the potential at which the passive film breaks down, E_b, where contributions to the current density are controlled by a mixture of kinetics and diffusion. Above the breakdown potential Souto et al. observe a Cu surface dominated by pit corrosion. It is observed, from Fig. S1, that a freshly polished Mg foil in EtMgBr has a E_b of about 250 mV (1st cycle electrodissolution overpotential due to passivation); since we are above this potential for the applied potentials used for Fig. 1a we believe that we are in the mixed kinetic and diffusion controlled regime. We used the current equations established for dissolution nucleation and growth, which are provided in the supplementary information, to fit the experimental data in Fig 1a (dashed traces). The fit parameters for the transient models are provided in Table S1. The best fits were achieved when the total contribution to the current included both the kinetic and diffusion controlled transient models. Based upon these equations the current that is calculated is due to kinetic controlled pitting at short times whereas hemispherical diffusion processes dominate at long times.

The data in Fig. 1b is a magnified view of the current density in the time region from 0 – 100 seconds at the three different overpotentials examined. The figure shows during each potential hold there appears to be a period of quiescence, a time before substantial current begins flowing. This period appears to be greatest for the lowest overpotential step (500 mV) and approximately the same for the two higher overpotentials. In point of fact, the initial interval of time at the onset of corrosion is known as the induction time and is an inherently stochastic process[30]. Additionally, when the thickness of the oxide layer is controlled, although a

decrease in the induction times is observed with an increase in the potential applied above E_b , for a Cu electrode in an aqueous electrolyte, the response is non-linear [29]. The fact that the initial current flow does not linearly correlate to the potential applied is indicative of the complexity of the competing reactions that occur upon initially applying a potential to a fresh Mg surface. As Mg is an active metal and known to form a passivating oxide layer and corrode in the presence of halides, we infer that these features are reflected in the transient behaviors seen in these data. In this model, polarization of the Mg foil working electrode toward dissolution potentials causes a localized breakdown in the oxide layer leading to an attack on the Mg surface by bromide (possibly in the form of $EtMgBr_2^{-1}$) [31]. The current flow, therefore, is hindered due to the necessity of an initial breakdown of this passivating layer to occur, and further raises the question of how the structure of the electrode changes in result. The data presented immediately below address these critical questions.

In order to further examine the putative depassivation behavior inferred from the voltammetry, we obtained SEM images (Fig. 2) from the three Mg metal foils following emersion at the three different potentials. The images show the Mg foil is decorated by pits following the potential excursion described above. Charge passed during the potential holds correlates directly with the number of pits as measured from the SEM images yet average, observable pit size remains the same within error which emphasizes the strong effect of potential upon nucleation yet diffusion control pit growth (Fig. S2). These data clearly reveal pitting dynamics mediate the metal dissolution and highlights a morphological embodiment for the induction time effects seen in Fig. 1. It can also be seen in Fig. 2 that the pits are weakly aligned with the grooves created by the polishing process. A sample with pits more strongly aligned with the grooves is shown in Fig. S3 along with the Fast Fourier Transform of the corresponding

micrograph that shows a high intensity line perpendicular to the grooves in the original micrograph, indicating that the pits are both parallel to the grooves and have irregular spacing. We also found at the macro scale that the pits were clustered in regions of higher mechanical stress, such as the area near the O-ring or regions where the foil was buckled. This suggests that a more favorable path to film breakdown occurs in regions of thinner, or less-protecting films (e.g. as due to surface defects or stress). Similarly to this system it has been shown for other magnesium systems that regions of breakdown sites increase with anodic current density [32]. The potentiostatic stripping experiments highlight the initial state characteristics of the anode surface and maintain a constant potential surface when passivation breakdown occurs. As we show below, repeated potentiostatic stripping and deposition cycles mitigate sample-preparation history dependences while crystallographic dependences are enhanced by the inherent electrochemical reaction dynamics of the system.

The temporal evolution of the electrochemical cycling behavior of bulk Mg electrodes is illustrated in the data presented in Fig. 3. Fig. 3a gives plots of the electrochemical data obtained from cycling at three different limiting potential ranges: slightly past E_b , moderately into the mixed control region, and at a high overpotential. The dash trace is for an electrode cycled between -/+ 300 mV , in which the potential was first held at -300 mV for 15 minutes and then switched to +300 mV for 15 minutes, repeating for 10 cycles. The same cycling procedure was used for the -/+ 500 mV (solid trace) and -/+ 700 mV cases (dash dot trace) shown in the figure. In a manner similar to what is observed in Fig. 1, the current density in both the anodic and cathodic potential steps increases with the magnitude of the potential applied (versus a Mg reference). The data in Fig. 3b plots the ratio of the integrated area for the deposition over dissolution step for each of the 10 cycles (presented as a percentage). It should be noted that for

all but one cycle, dissolution is favored. In fact, for the -/+ 300 mV and -/+ 700 mV cases, dissolution is moderately more dominant than deposition for the first few cycles. The origin of this asymmetric current scaling is not completely understood. It has been observed by others that unless the Mg metal surface is activated in the electrolyte it will be covered in a passivating film composed of environmental contaminants [14] and though deposition is not completely blocked, it is hindered by this film. Even so, in the current case, it remains true that the time-based measure always more efficiently removes Mg from the bulk anode than the deposition step adds to it. The data discussed in the sections that follow suggest an explicit mechanism responsible for more facile dissolution.

The data presented in Figs. 4(a-c) are SEM images measured for electrodes cycled at the different potential ranges after the completion of 10 full deposition/dissolution cycles. These data establish that variations in the potential produce different surface morphologies. In each case, albeit with different scales of texturing, the cycling leads to the occurrence of anisotropic Mg structures on the surfaces of the bulk electrodes. Although other structures are formed, many of the structures evidenced suggest an anisotropic pattern of growth/etching of a specific preferred orientation of these hexagonal close packed (hcp) Mg grains. This finding has precedent in that Hill et al. observed that, under specific conditions, in ether solvents containing alkyl halides a major fraction of the pits formed on Mg metal are anisotropically etched when an {0001} oriented single crystal was used [33]. The crystallographic texture of the foil samples was examined for this reason; X-ray diffraction studies (Fig. S4) show that the Mg foils used for our experiments are in fact preferentially oriented along the {0001} direction. As the data in Fig. 4 illustrate, the anisotropy that occurs after multiple cycles, after ending at dissolution potentials, is broadly distributed across the sample surface and comprise mainly the walls of Mg crystallites

deposited with a preferred {0001} oriented texture. Geometric analysis of the structures in Fig. 4b produces angles of 63.16° +/-4.95 and 121.5° +/-6.95, confirming roughly vertically aligned {0001} hexagonal crystals typical of an hcp lattice. In fact, the quasi-hexagonal morphology deposits are the only anisotropic texture observed, regardless of order of the potential holds, galvanostatic vs. potentiostatic cycling, or even substrate texture (SI Figs. 5-7). Others have observed dissolution differences between planes of magnesium [34-38]. Liu et al. suggested that the activation energy of dissolution increases as the packing density of the plane increases for the hexagonal close-packed (hcp) magnesium [35]. Planes perpendicular to the {0001} basal plane, however, have lower packing densities and by this mode should have a more favorable dissolution. In point of fact, the literature in [34, 36] contains some contradictions regarding the corrosive dissolution behaviors of the {0001} plane of Mg. Song et al. [36] observed that in 0.01 M NaCl the {0001} plane is most resistant to dissolution, yet McCall et al. [34] observed that in 0.01 M NaCl/0.0001 M dichromate solution the {0001} plane is the least resistant when compared to low-index prismatic planes (e.g. the {10-10} plane). Song et al. proposed that this contrast is due to the fact that growth of surface films can vary markedly on the different planes and also vary in different electrolytes [36]. We believe the current data support this picture of corrosion due to halide species and that the structures observed upon cycling likely result from passive films that vary in structure for the different Mg hcp planes, a factor resulting in both an anisotropic stripping and subsequent replating of the Mg. Logical inferences suggest an oxide speciation is likely for the passive films that mediate this rate-structure correlation.

To test this assumption, the surface speciation of three different Mg foil samples was determined by use of XPS. Plotted in Fig. 5 are the core level data measured in the O(1s), Br(3d), and the Mg(2p) binding energy regions, here recorded for a polished Mg foil (p), a Mg

foil working electrode stripped at +500 mV for 30 minutes (s), and a Mg foil working electrode after 10 cycles at -/+ 500 mV with the cycles terminated at the anodic potential limit (c). In order to minimize exposure to air, the Mg foils were transferred to the XPS instrument via a sealed transfer vessel. These data (as tabulated in Table 1) show the state of the surface of the Mg after processing by polishing in an inert atmosphere, electrochemical stripping, or potentiostatic cycling. The data in Fig. 5a show plots of the oxygen 1s binding energy region. The polished Mg foil sample shows the presence of mostly glovebox related surface contaminants, namely MgO and MgCO₃. The other samples contain lesser amounts of MgO, a result of removal of the initial surface oxide during electrochemical cycling. The increase in the peak around 533 eV observed for the stripped and cycled experiments, is due to an increase in oxygen containing species on the surface of the Mg foil (Mg(O)X) most likely as a result of solvent, THF, decomposition. We note that here X does not refer to a halide but rather to an unknown species. The data in Fig. 5b are plots in the region of the Br 3d core level binding energy. The results for the stripped and cycled Mg foils show the presence of a distinct MgBr, speciation. According to one of the dissolution reactions proposed by Aurbach et al. [31], MgBr, is a corrosion product and, since it has low solubility in THF, forms as a precipitate. As corrosion proceeds, corrosion products build up [36], especially in the form of halide salts. Even though MgBr, accumulates during both hemispherical pitting and anisotropic pitting, the lack of non-passivated Mg {10-10} planes upon initial stripping precludes the dismissal of MgBr, contributing to the anisotropic stripping. We note that the additional peaks present in the spectra given in Fig. 5b are likely due to the KLL Auger excitations of Mg and a bulk Mg plasmon (at 67.4, 73.6 and 70.0 eV respectively) [39, 40]. The data in Fig. 5c show plots of the Mg 2p core level binding energy region. The polished Mg foil sample has peaks near where Mg^0 and MgO

binding energies are expected. When the Mg foil is stripped or cycled, the electrolyte decomposition and corrosion products build up on the surface and the Mg⁰ peak is reduced in intensity. Not surprisingly, the surface film formed during electrochemical processes contains mostly decomposition/corrosion products.

To further establish the character and morphology of passive films that likely mediate the anisotropic growth/dissolution behaviors established above, FIB was used in conjunction with HIM to garner a structural understanding of the films from high resolution cross-sectional images. Such images provide mechanistic insights into the process of stripping and deposition of Mg. Figs. 6a and 6c present HIM images taken at normal incidence, each of typical Mg structures formed during the potentiostatic cycling (at -/+ 500 mV, 20 cycles, for 15 minutes per half cycle) on a Mg foil working electrode. There are several observable morphologies including smooth areas, quasi-hexagonal symmetry crystals, and, as previously seen in the images in Fig. 4, nested hexagonal motifs. The smooth areas represent non-activated regions of the original, passivated surface of the Mg foil. Unlike previous examples, this sample processing was ended on a deposition half-cycle, resulting in many quasi-hexagonal structures with varying degrees of nesting. Two distinct quasi-hexagonal structures are evident, with apparently different degrees of filling by Mg. Each types of morphology was cross-sectioned via FIB milling and imaged by HIM. Figs. 6b and 6d show views of specific cross-sections from 6a and 6c representing the nested and non-nested structures, respectively. Fig. 6b shows that the anisotropic stripping in the Grignard electrolyte often does not completely remove the Mg deposited during the previous half-cycle, as manifested in the lateral discontinuity seen at the top of the structure (combined with the relatively uniform interior) and the very thin (~ 10 nm) thin films of oxidized material. Most notably, both cross-sections reveal interstices that develop during deposition. The presence

of interstices (sometimes referred to as voids or pores in literature) is common in electroplating and results from multiple grains growing into one grain to begin columnar growth [41]. As evidenced by the relatively large, uniform growth of the crystal in Fig. 6d, deposition is also preferentially oriented to the {0001} plane. This deposition orientation has never been observed for EtMgBr and is likely due to a combination of homoepitaxial growth and surface-oxide-limited diffusion of the Mg.

Fig. 7 depicts our schematic interpretation of the complex growth dynamics that are occurring in this system. Upon initial stripping of the oxide layer formed after polishing, nucleated pitting occurs in a relatively isotropic manner due to localized failures of the relatively passive surface films that remain. Switching to negative potentials initiates homoepitaxial growth on the now activated and generally {0001} textured surface planes exposed by the pits, leading to the formation of microcrystalline hexagonal motif deposits (shown as orange). It has been hypothesized that RMg⁺ species cause oxidation of THF at the surface due to the Lewis acidity of RMg⁺ [19], and therefore rapid passivation from the byproducts of the decomposition of THF (along with MgBr₂) likely occurs all Mg surfaces. Once the hexagonal passivated structures are formed, these same crystals tend to selectively strip from the substrate (Fig. 7c). Other passivated surfaces become activated but are primarily localized in these and adjoining areas of the substrate. Subsequent deposition then follows upon the low overpotential, 'fresh' surfaces created frequently within the residual structures from past deposition/passivation/stripping sequences. Extensive cycling exacerbates this effect, and as shown, causes very large 50 micron or taller columns to protrude from the electrode surface even after a relatively short sequence of cycles (Fig S8). The concern following from this, similar to

issues caused by lithium metal anode dendrites [8], is that these structures would eventually grow large enough to create an electrical short in a full cell.

4. Conclusions

Passivation and corrosion processes play a crucial role in the electrochemical behavior of bulk Mg metal anodes using a non-aqueous Grignard electrolyte. Morphological characterization of the Mg working electrode after electrochemical reactions shows the formation of corrosion pits and anisotropically etched hexagonal Mg structures. Observation of the Mg working electrode after extensive deposition and dissolution cycles reveals the formation of isolated columnar structures. Although they do not have as high of an aspect ratio nor are as numerable as the dendrites formed on Li metal anodes, these structures hold the possibility of extending toward the cathode and causing battery failure with a potential for the loss of electroactive Mg. These results suggest that careful consideration of the possible anisotropy of both the deposition and the stripping of Mg is necessary for Mg to be a viable candidate for use as an anode in a rechargeable battery.

Acknowledgements

This work was supported as part of the Joint Center for Energy Storage Research, an Energy Innovation Hub funded by the U.S. Department of Energy, Office of Science, Basic Energy Sciences. This work was carried out in part in the Frederick Seitz Materials Research Laboratory Central Facilities, University of Illinois at Urbana-Champaign and in the Department of Physics, Bielefeld University.

References

- [1] I. Shterenberg, M. Salama, Y. Gofer, E. Levi, D. Aurbach, MRS Bulletin, 39 (2014) 453-460.
- [2] P. Saha, M.K. Datta, O.I. Velikokhatnyi, A. Manivannan, D. Alman, P.N. Kumta, Progress in Materials Science, 66 (2014) 1-86.
- [3] D. Aurbach, G.S. Suresh, E. Levi, A. Mitelman, O. Mizrahi, O. Chusid, M. Brunelli, Advanced Materials, 19 (2007) 4260-4267.
- [4] H.D. Yoo, I. Shterenberg, Y. Gofer, G. Gershinsky, N. Pour, D. Aurbach, Energy & Environmental Science, 6 (2013) 2265.
- [5] W. Xu, J. Wang, F. Ding, X. Chen, E. Nasybulin, Y. Zhang, J.-G. Zhang, Energy & Environmental Science, 7 (2014) 513-537.
- [6] M.S. Park, S.B. Ma, D.J. Lee, D. Im, S.-G. Doo, O. Yamamoto, Scientific reports, 4 (2014).
- [7] N. Jayaprakash, S.K. Das, L.A. Archer, Chemical communications, 47 (2011) 12610-12612.
- [8] I. Yoshimatsu, T. Hirai, J.i. Yamaki, Journal of the Electrochemical Society, 135 (1988) 2422-2427.
- [9] R. Khurana, J. Schaefer, L.A. Archer, G.W. Coates, Journal of the American Chemical Society, (2014).
- [10] K.J. Harry, D.T. Hallinan, D.Y. Parkinson, A.A. MacDowell, N.P. Balsara, Nature materials, 13 (2014) 69-73.
- [11] N. Schweikert, A. Hofmann, M. Schulz, M. Scheuermann, S.T. Boles, T. Hanemann, H. Hahn, S. Indris, Journal of Power Sources, 228 (2013) 237-243.
- [12] J.K. Stark, Y. Ding, P.A. Kohl, Journal of The Electrochemical Society, 160 (2013) D337-D342.
- [13] M.Z. Mayers, J.W. Kaminski, T.F. Miller III, The Journal of Physical Chemistry C, 116 (2012) 26214-26221.

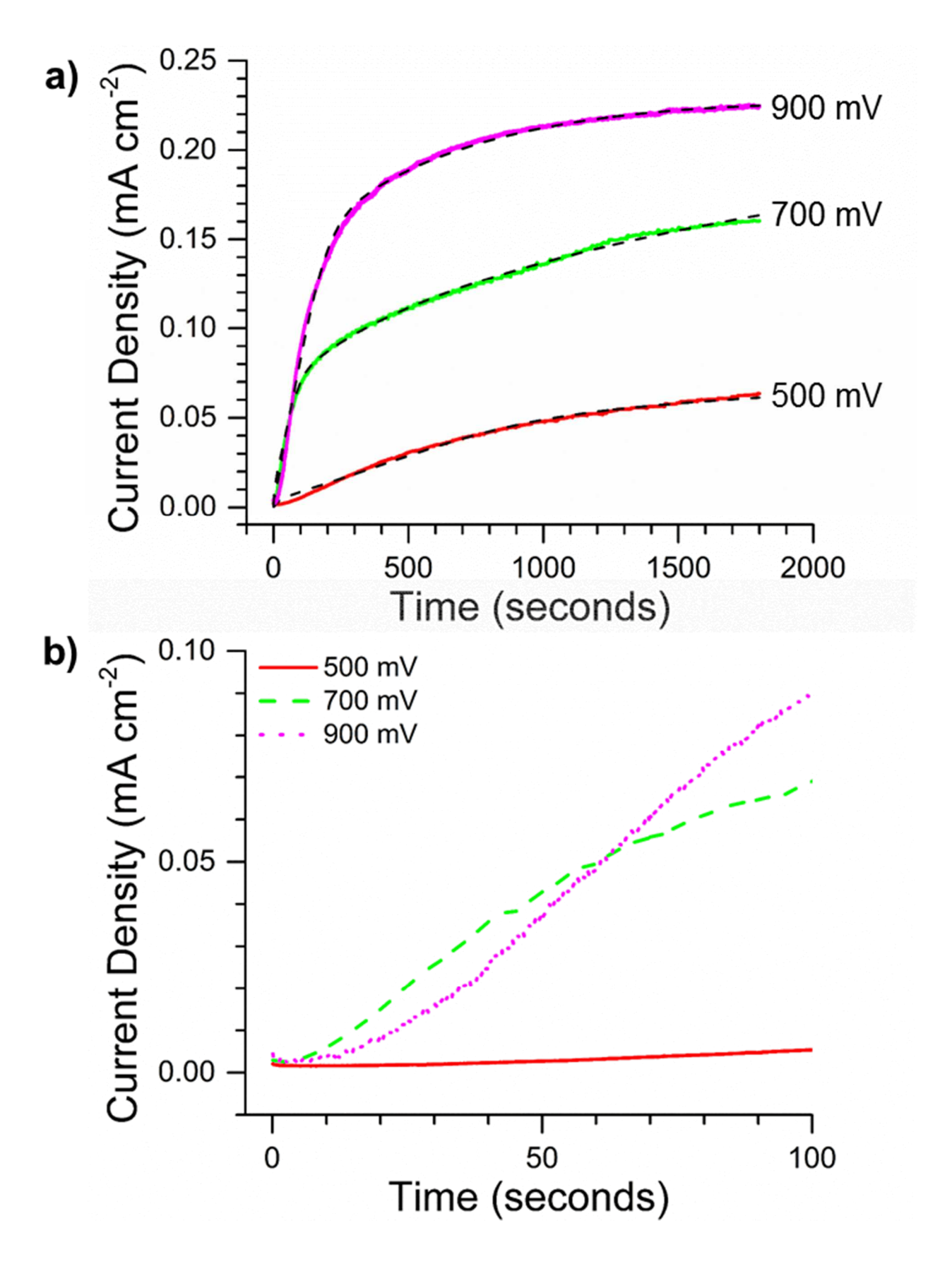
- [14] Z. Lu, A. Schechter, M. Moshkovich, D. Aurbach, Journal of Electroanalytical Chemistry, 466 (1999) 203-217.
- [15] T.D. Gregory, R.J. Hoffman, R.C. Winterton, Journal of the Electrochemical Society, 137 (1990) 775-780.
- [16] J. Zhu, Y. Guo, J. Yang, Y. Nuli, F. Zhang, J. Wang, S.-i. Hirano, Journal of Power Sources, 248 (2014) 690-694.
- [17] Z. Zhao-Karger, J.E. Mueller, X. Zhao, O. Fuhr, T. Jacob, M. Fichtner, RSC Advances, 4 (2014) 26924.
- [18] T. Liu, Y. Shao, G. Li, M. Gu, J. Hu, S. Xu, Z. Nie, X. Chen, C. Wang, J. Liu, Journal of Materials Chemistry A, 2 (2014) 3430.
- [19] C.J. Barile, R. Spatney, K.R. Zavadil, A.A. Gewirth, The Journal of Physical Chemistry C, 118 (2014) 10694-10699.
- [20] Y. Cheng, T. Liu, Y. Shao, M.H. Engelhard, J. Liu, G. Li, Journal of Materials Chemistry A, 2 (2014) 2473.
- [21] P. Bian, Y. NuLi, Z. Abudoureyimu, J. Yang, J. Wang, Electrochimica Acta, 121 (2014) 258-263.
- [22] S.Y. Ha, Y.W. Lee, S.W. Woo, B. Koo, J.S. Kim, J. Cho, K.T. Lee, N.S. Choi, ACS applied materials & interfaces, 6 (2014) 4063-4073.
- [23] R.E. Doe, R. Han, J. Hwang, A.J. Gmitter, I. Shterenberg, H.D. Yoo, N. Pour, D. Aurbach, Chemical communications, 50 (2014) 243-245.
- [24] A. Benmayza, M. Ramanathan, T.S. Arthur, M. Matsui, F. Mizuno, J. Guo, P.-A. Glans, J. Prakash, The Journal of Physical Chemistry C, 117 (2013) 26881-26888.
- [25] J. Muldoon, C.B. Bucur, A.G. Oliver, J. Zajicek, G.D. Allred, W.C. Boggess, Energy & Environmental Science, 6 (2013) 482.
- [26] Z. Zhao-Karger, X. Zhao, O. Fuhr, M. Fichtner, RSC Advances, 3 (2013) 16330.

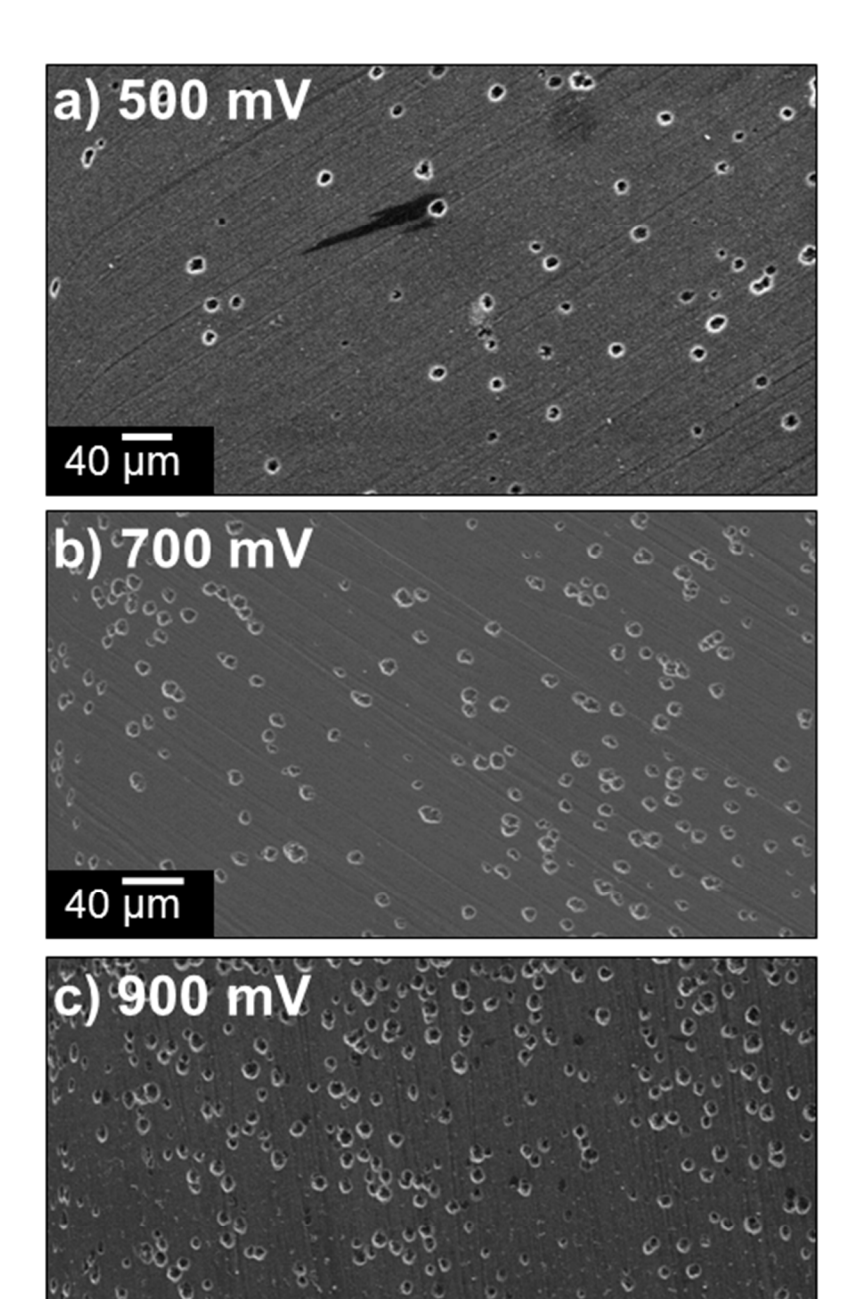
- [27] Y.-s. Guo, F. Zhang, J. Yang, F.-f. Wang, Y. NuLi, S.-i. Hirano, Energy & Environmental Science, 5 (2012) 9100-9106.
- [28] R. Zhang, X. Yu, K.-W. Nam, C. Ling, T.S. Arthur, W. Song, A.M. Knapp, S.N. Ehrlich, X.-Q. Yang, M. Matsui, Electrochemistry Communications, 23 (2012) 110-113.
- [29] R.M. Souto, S. González, R.C. Salvarezza, A.J. Arvia, Electrochimica Acta, 39 (1994) 2619-2628.
- [30] T. Shibata, T. Takeyama, Nature, 260 (1976) 315-316.
- [31] D. Aurbach, M. Moshkovich, A. Schechter, R. Turgeman, Electrochemical and Solid-State Letters, 3 (2000).
- [32] G. Song, A. Atrens, D.S. John, X. Wu, J. Nairn, Corrosion Science, 39 (1997) 1981-2004.
- [33] C.L. Hill, J.B. Vander Sande, G.M. Whitesides, The Journal of Organic Chemistry, 45 (1980) 1020-1028.
- [34] C. McCall, M. Hill, R. Lillard, Corrosion engineering, science and technology, 40 (2005) 337-343.
- [35] M. Liu, D. Qiu, M.-C. Zhao, G. Song, A. Atrens, Scripta Materialia, 58 (2008) 421-424.
- [36] G.-L. Song, Z. Xu, Corrosion Science, 54 (2012) 97-105.
- [37] K.S. Shin, M.Z. Bian, N.D. Nam, JOM, 64 (2012) 664-670.
- [38] R.S. Lillard, G.F. Wang, M.I. Baskes, Journal of the Electrochemical Society, 153 (2006) B358-B364.
- [39] J.C. Fuggle, L.M. Watson, D.J. Fabian, S. Affrossman, Journal of Physics F: Metal Physics, 5 (1975) 375.
- [40] M. Kurth, P.C.J. Graat, Surface and Interface Analysis, 34 (2002) 220-224.

[41] J.A. Abys, Palladium Electroplating, in: Modern Electroplating, John Wiley & Sons, Inc., 2010, pp. 327-368.

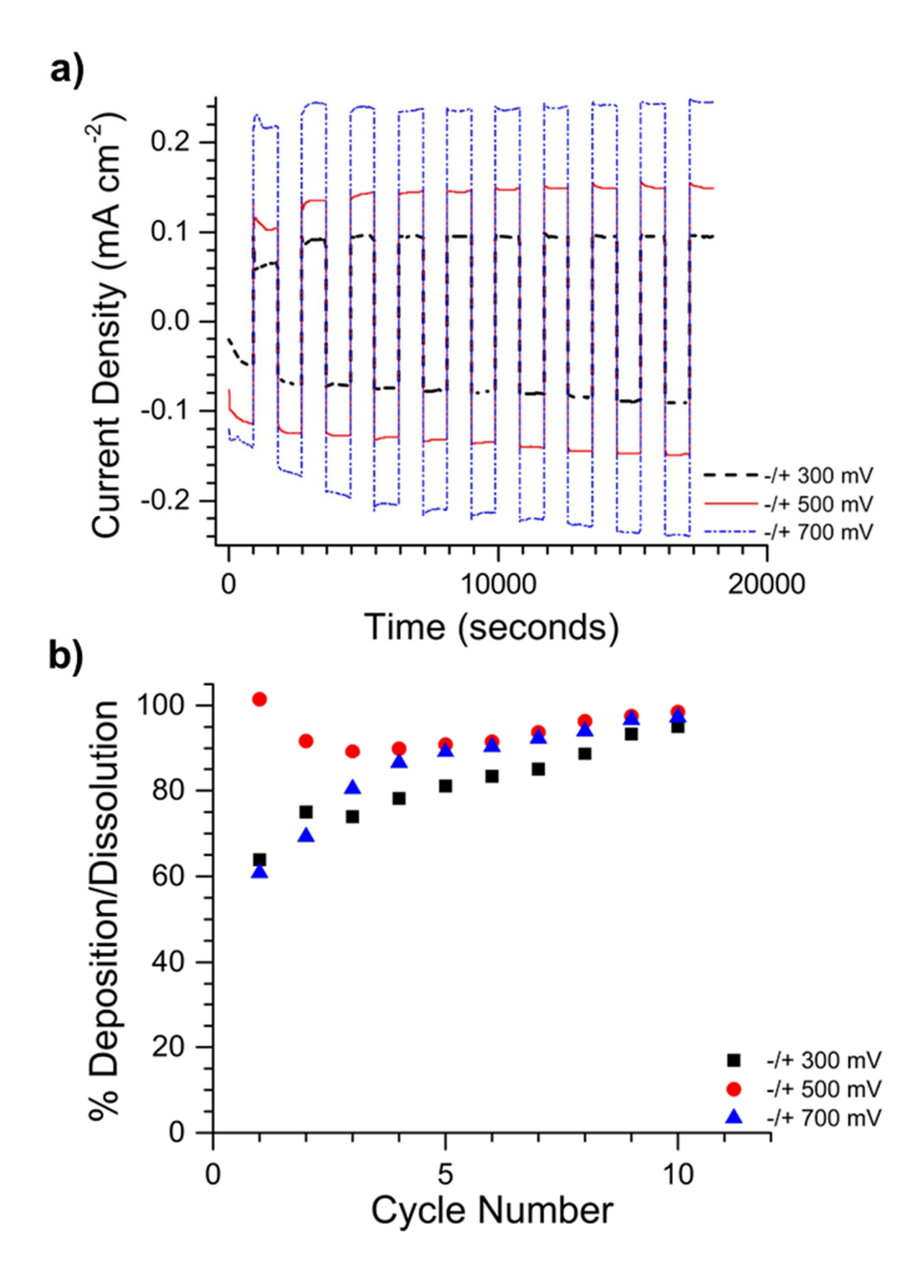
Region	Process	Peak Assignment	Binding Energy (eV)
O(1s)	1 100033	Assignment	Billiang Energy (CV)
0(10)	Polished	MgO	531.2
		MgCO ₃	533.2
	Stripped	MgO	531.0
		$MgCO_3/Mg(O)X$	533.1
	Cycled	MgO	531.0
		$MgCO_3/Mg(O)X$	533.2
Br(3d)			
	Polished	KLL MgO Mg bulk	68.2
		plasmon	71.1
		KLL Mg	74.0
	Stripped	$MgBr_2$	70.7
	Cycled	MgBr ₂	70.8
Mg(2p)			
	Polished	Mg ⁰	50.0
		MgO	51.6
	Stripped	Mg ⁰	50.1
		MgBr ₂ /MgO	51.6
	Cycled	Mg ⁰	50.1
		MgBr ₂ /MgO	51.7

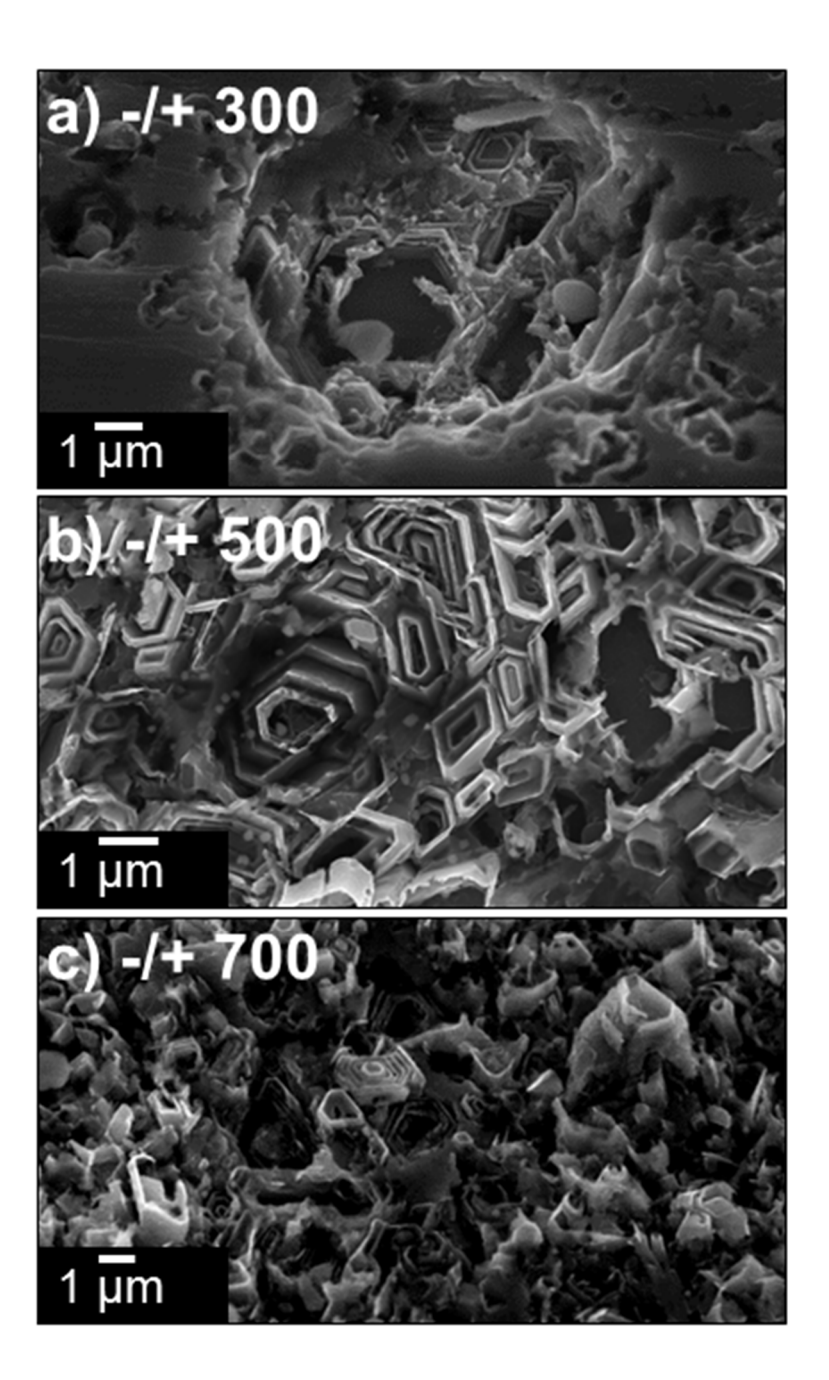
Table 1. Core level binding energies of processed Mg foils measured by XPS

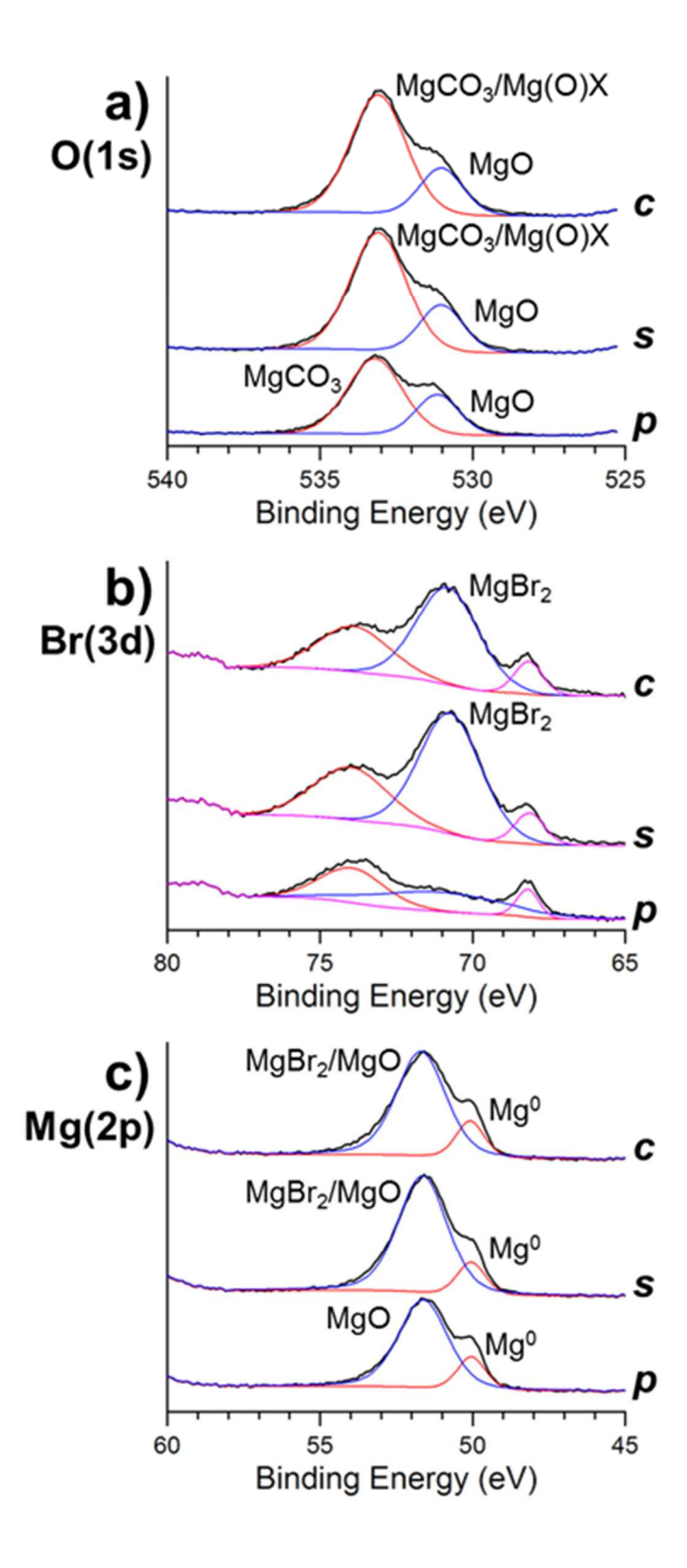


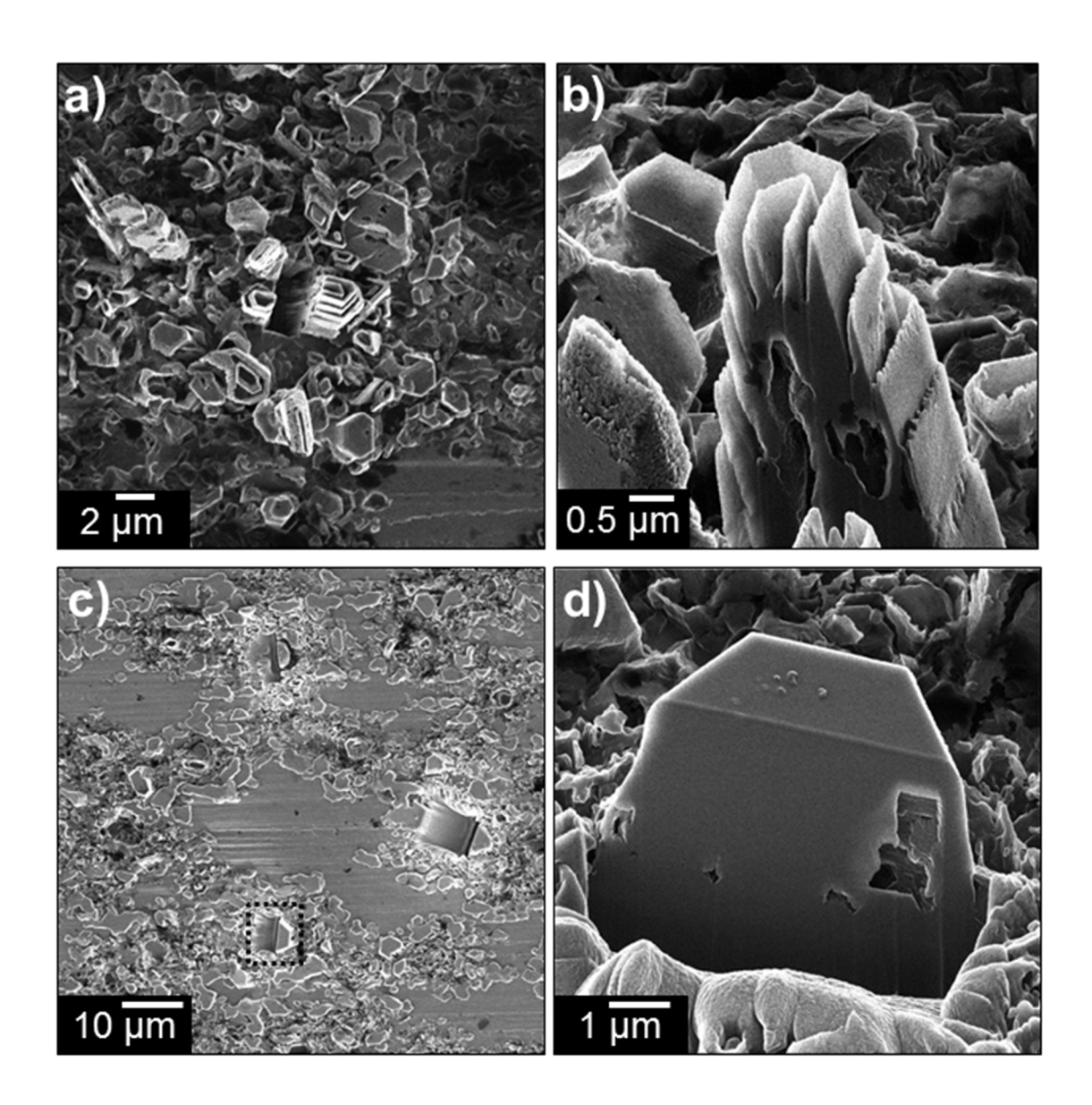


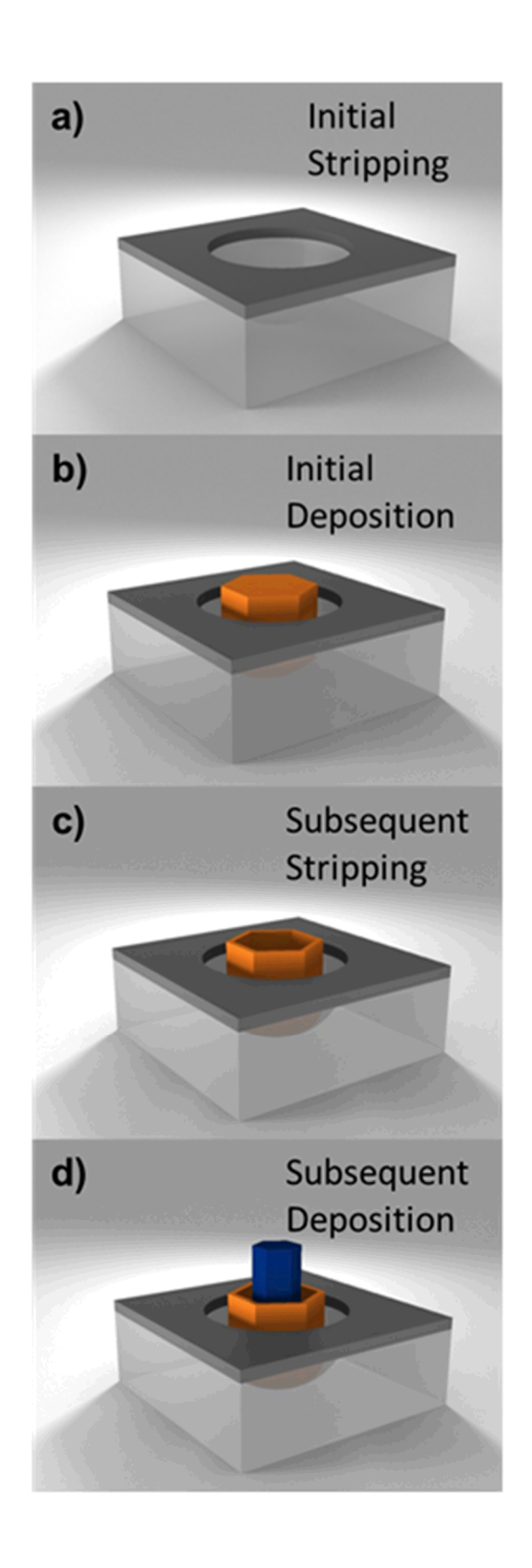
40 µm











Supporting Information

Potential (mV)	P ₄ (mA cm ⁻²) (10 ⁻⁴)	P ₅ (s ⁻²) (10 ⁻⁷)	P ₆ (mA s ^{1/2} cm ⁻²)	P ₇ (s ⁻¹) (10 ⁻⁶)
500	267.6 ± 1.1	19.99 ± 0.13	100 ± 70	8 ± 5
700	429.0 ± 0.9	2319 ± 10	26.71 ± 0.24	118.2 ± 1.3
900	895.8 ± 2.6	466.2 ± 1.3	8.963 ± 0.014	567.9 ± 1.9

Table S1. Fit parameters for current transient models

$$j_{t} = j_{c} + j_{d'}$$

$$j_{c} = P_{4}[1 - \exp(-P_{5}t^{2})]$$

$$j_{d'} = P_{6}t^{-1/2}[1 - \exp(-P_{7}t)]$$

$$P_{4} = zFk$$

$$P_{5} = \pi M^{2}N_{0}k'^{2}\rho^{-2}$$

$$P_{6} = zF\pi^{-1/2}D'^{1/2}\Delta c'$$

$$P_{7} = K'\pi D'N_{os}$$

$$K = (8\pi M\Delta c')^{1/2}\rho^{-1/2}$$

 j_c is the current density concerned with the corrosion of metal at the pits and defines the instantaneous nucleation and three-dimensional conical pit growth charge transfer control.

Where,

z is the charge number

F is the Faraday constant

k and k' are the apparent rate constants for pit growth in the directions perpendicular and parallel to the corroding surface plane, respectively

M and ρ are the atomic weight and the density of the metal, respectively

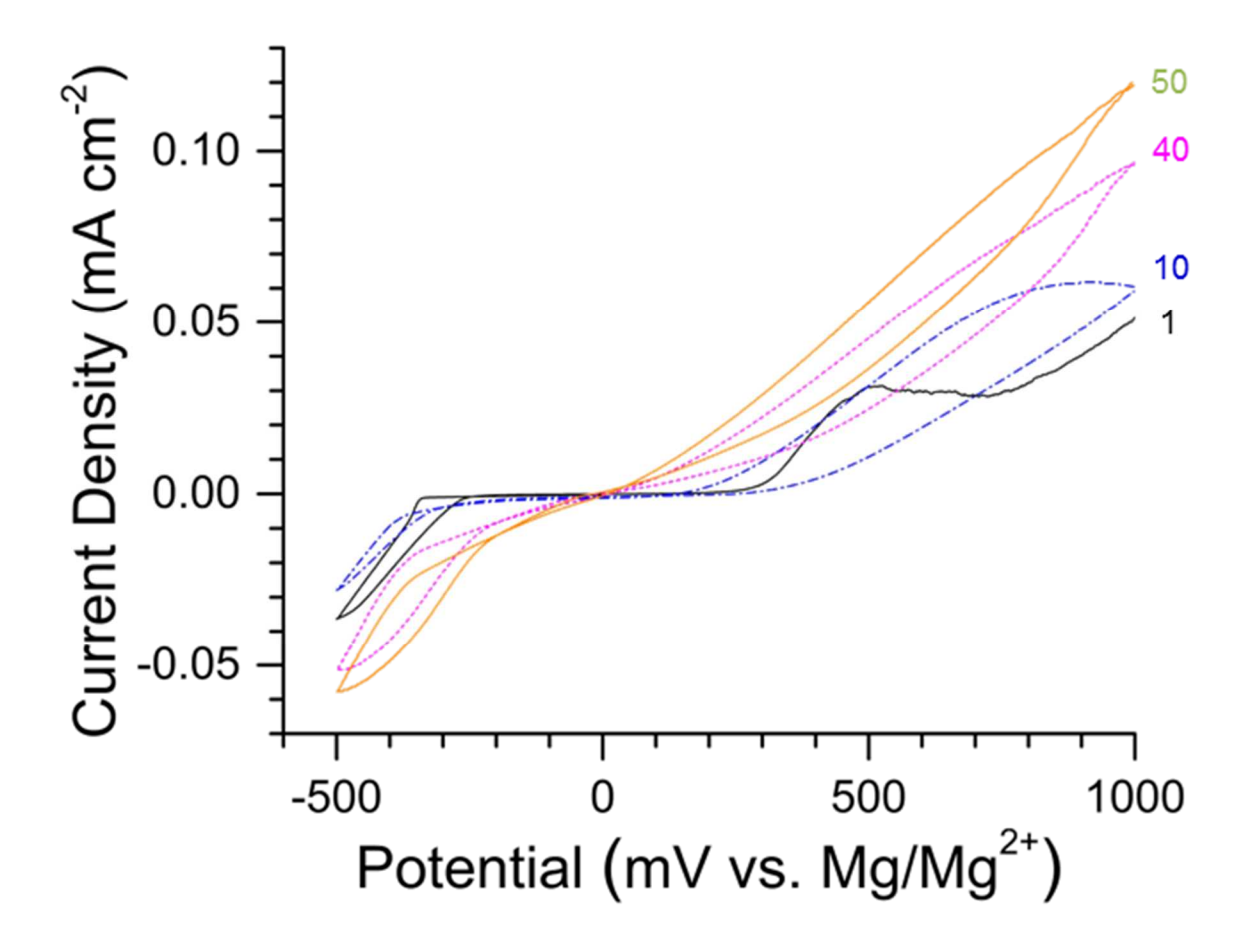
 N_0 is the number of sites available for pit nucleation

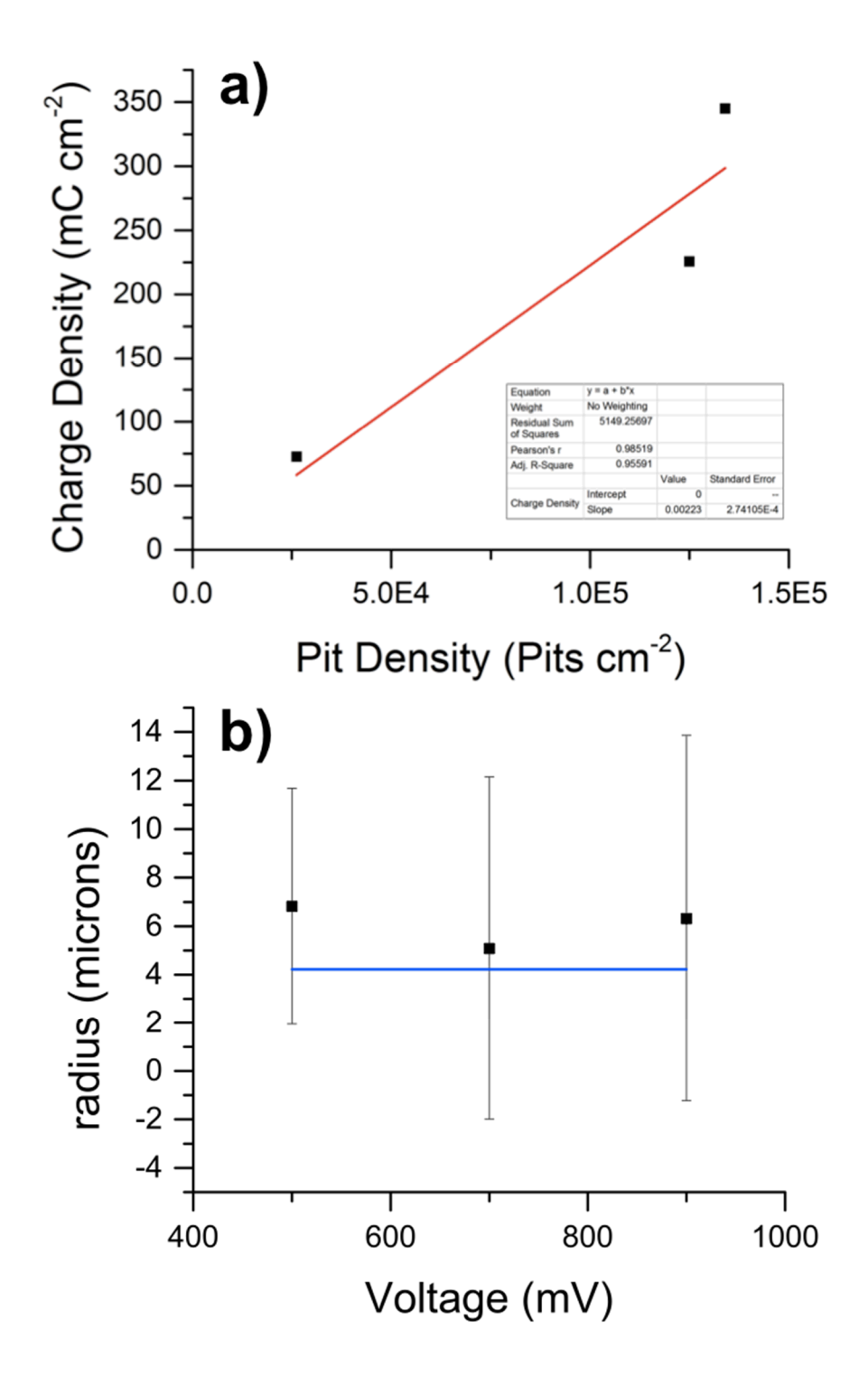
 $j_{d'}$ represents metal dissolution through a basic metal salt layer formed at certain regions of the electrode

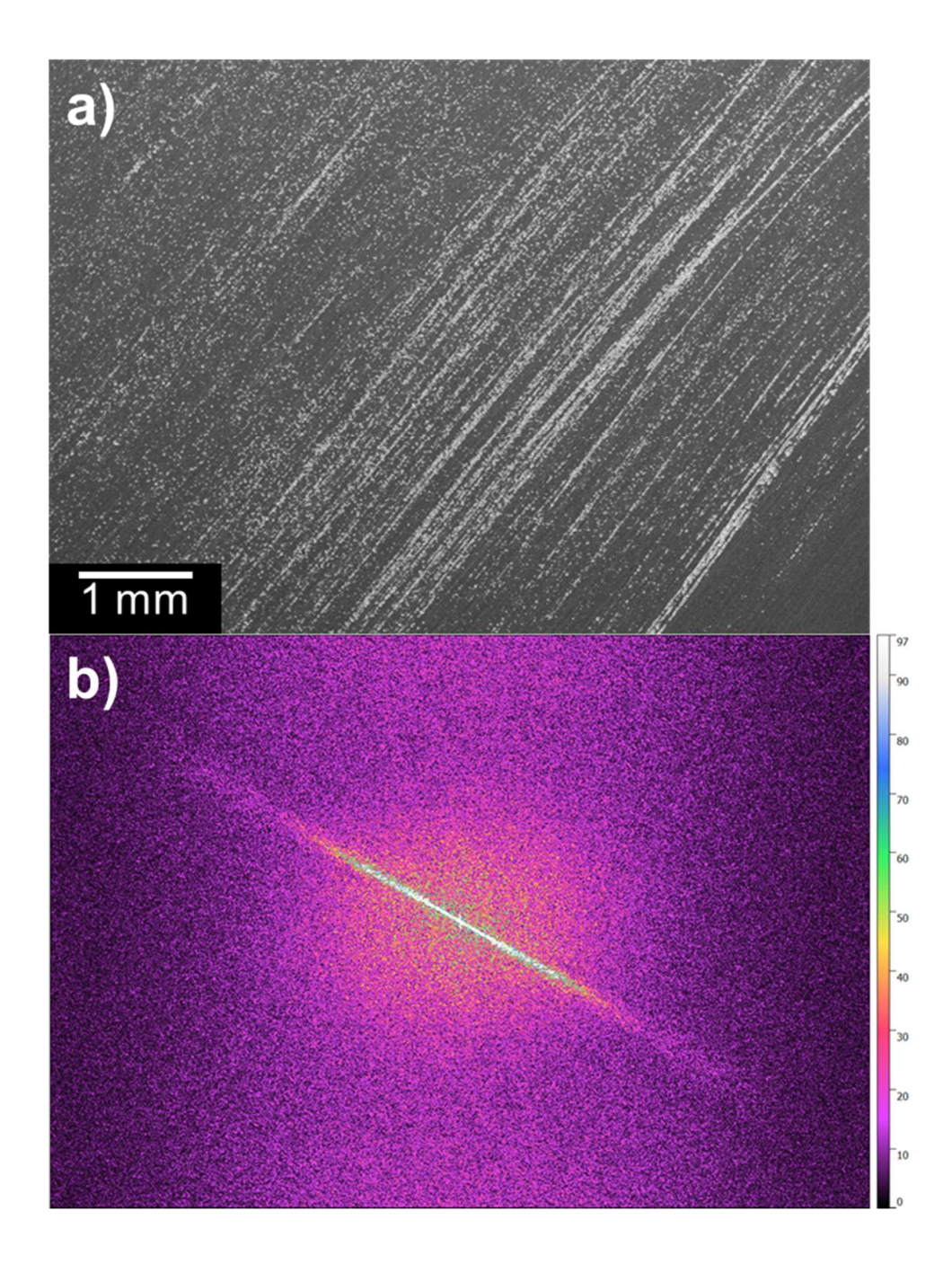
D' is the diffusion coefficient of the metal ions in the solution

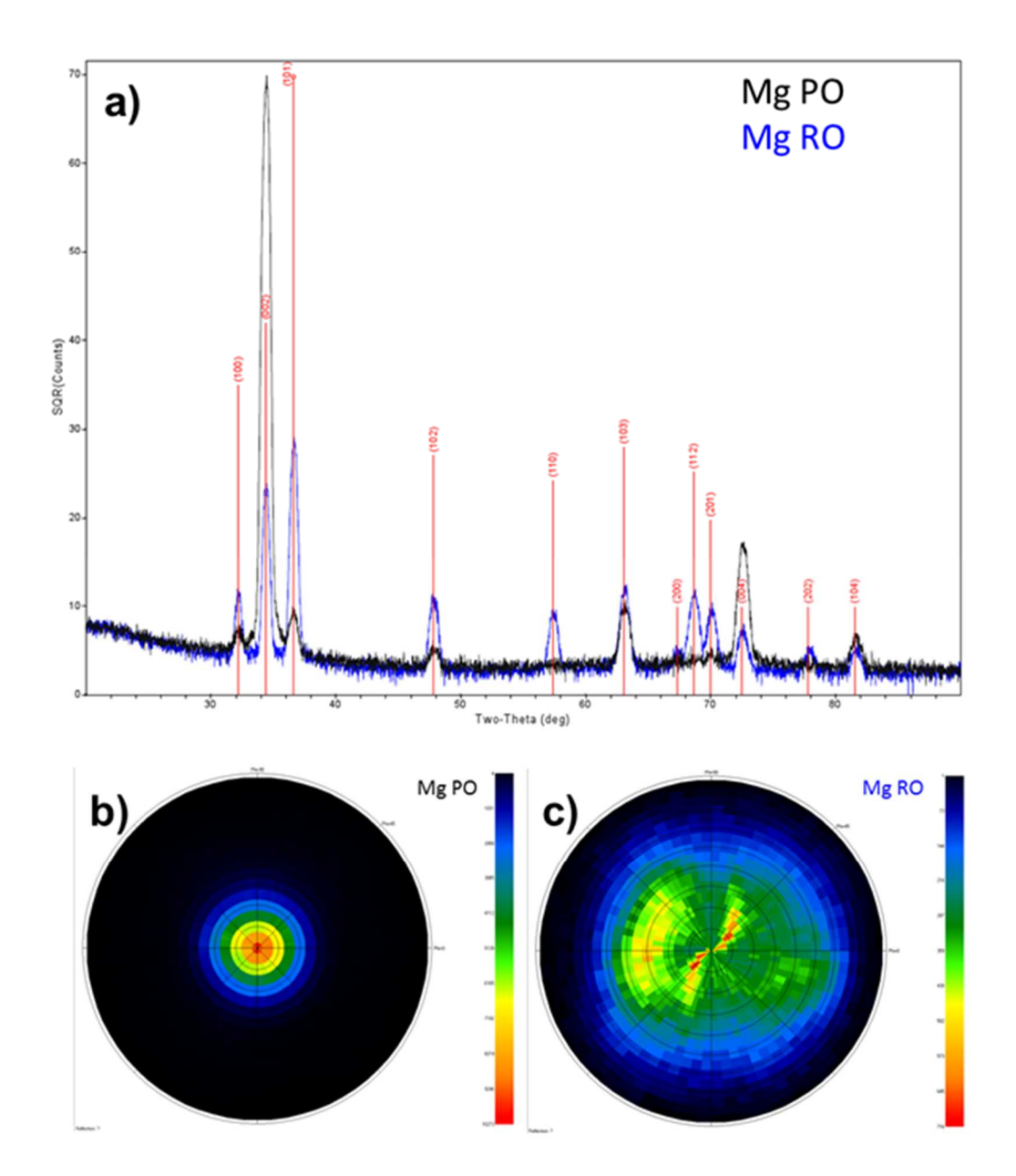
 Δc ' is the concentration gradient of the metal ionic species at the salt/solution interface

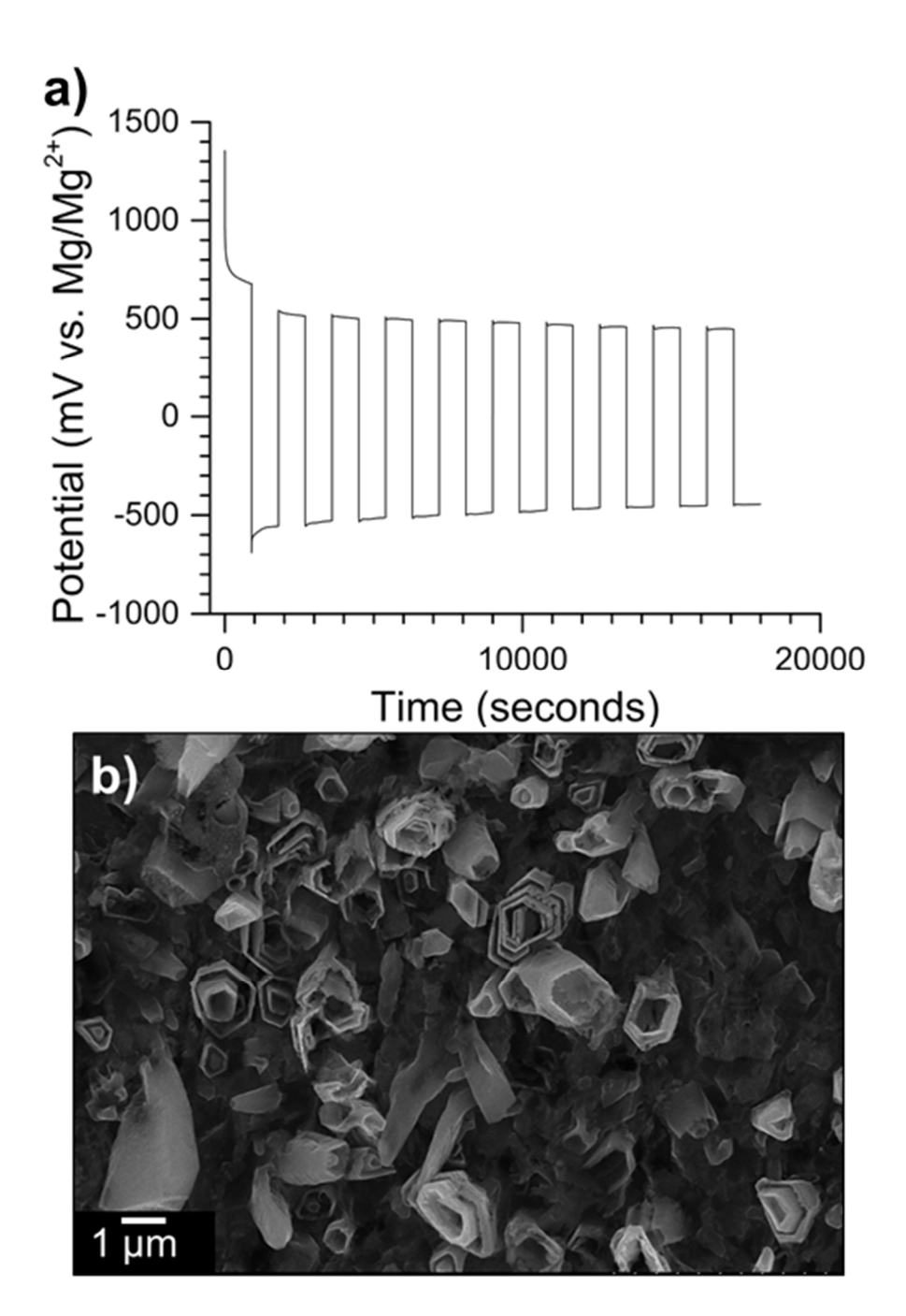
Nos stands for the number of sites for pit growth

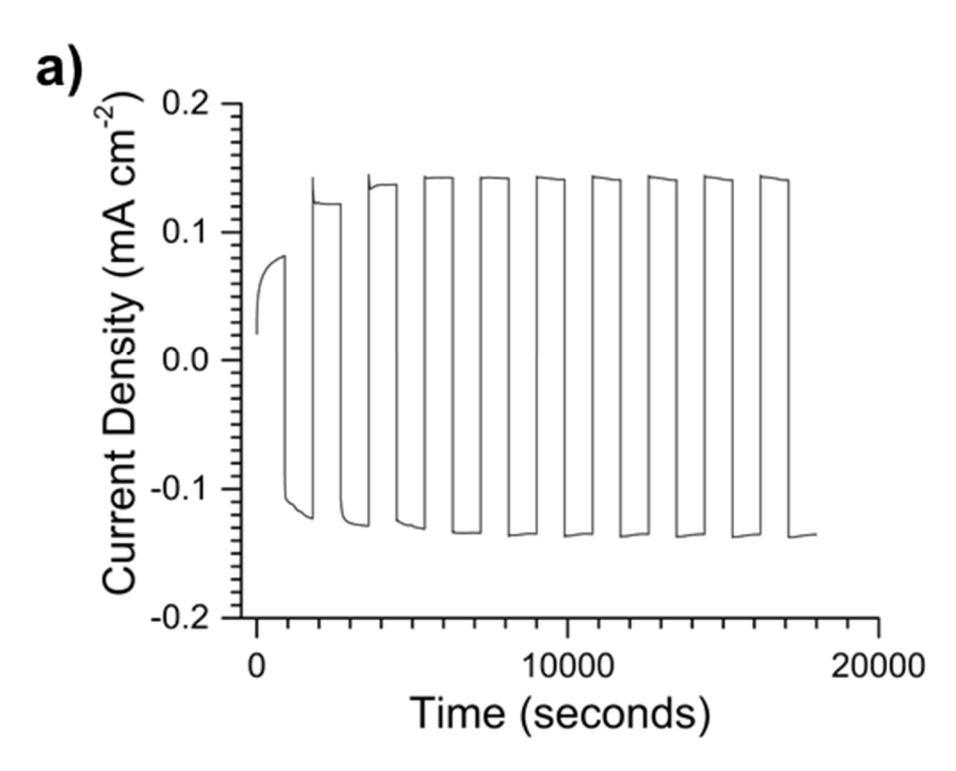


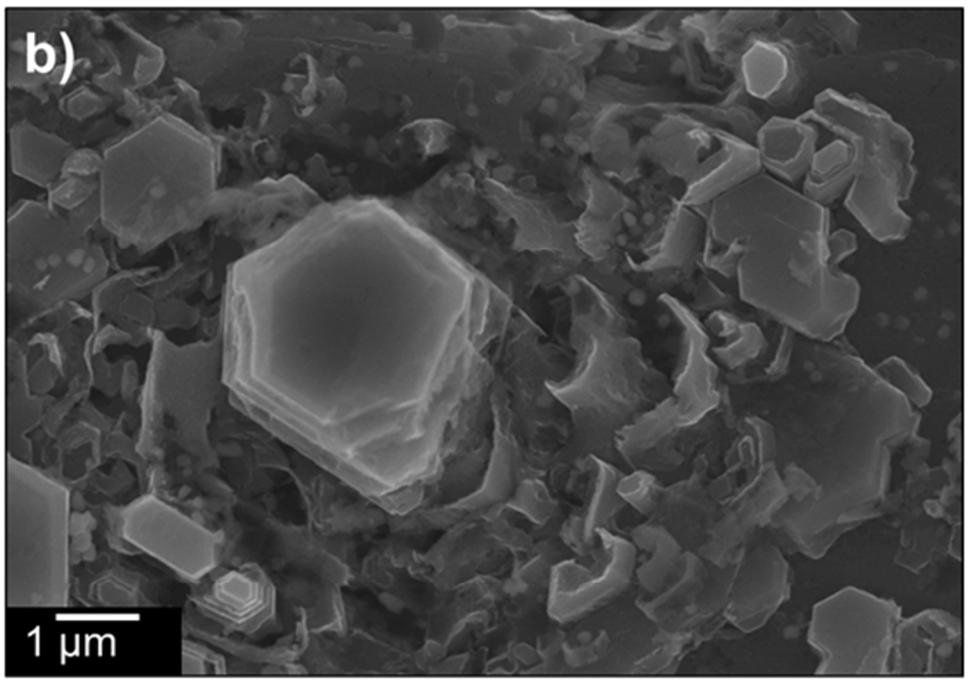


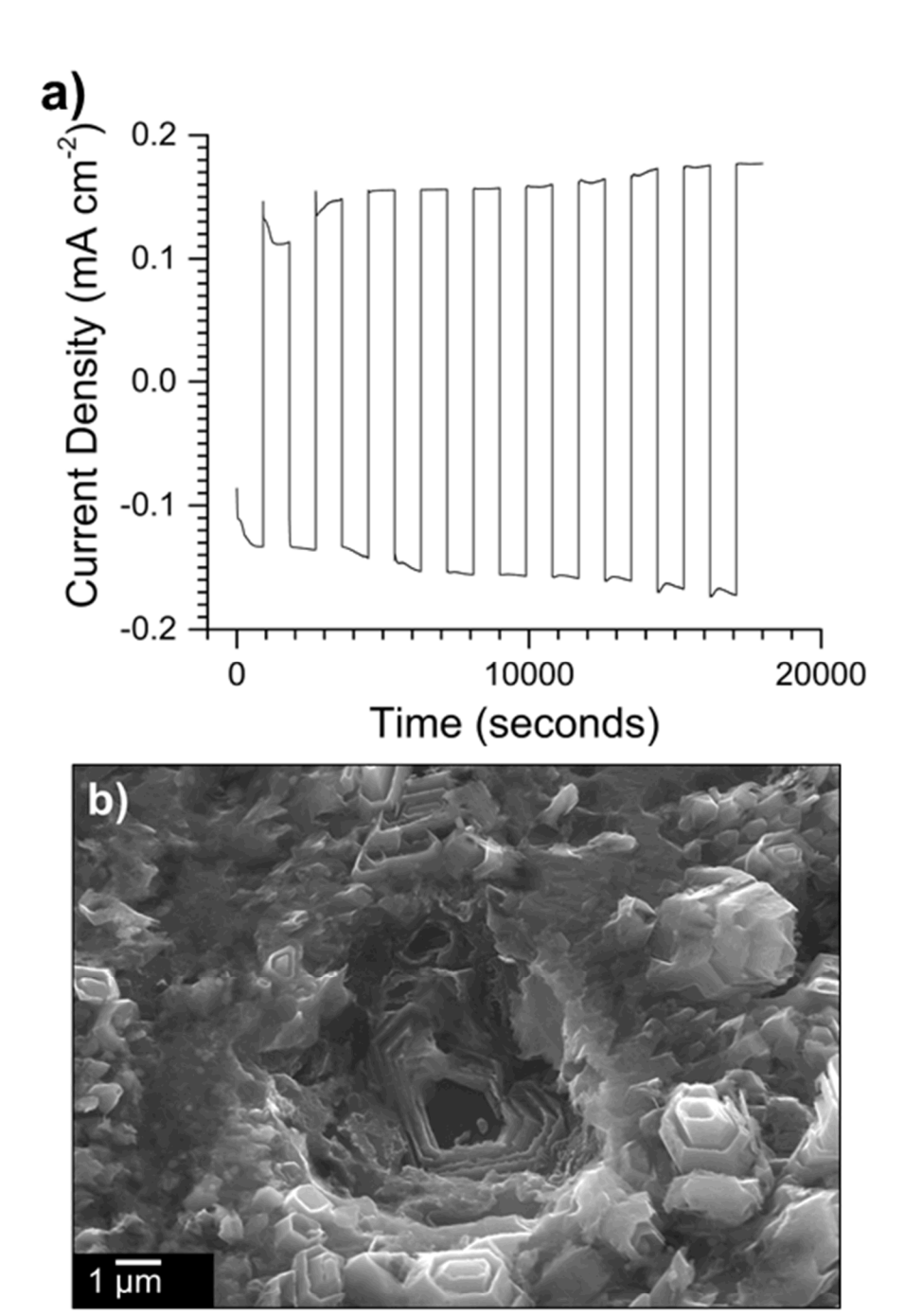


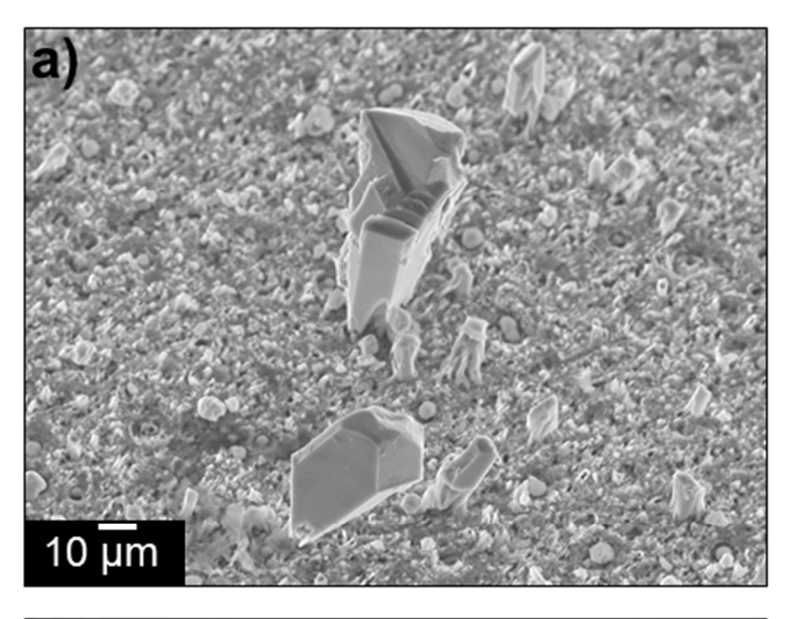


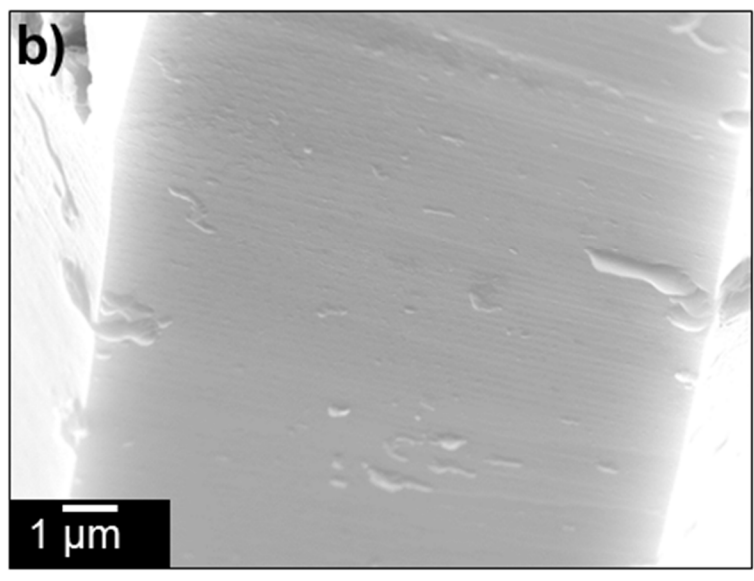












Main text figure captions

- **Fig. 1.** Current-time transients of polished Mg foils in EtMgBr at three different dissolution potential holds of (a) 500 mV, 700 mV, and 900 mV for 30 continuous minutes. (b) Magnification of the region between 0 − 100 seconds in (a). Counter and reference electrodes were polished strips of Mg ribbon.
- **Fig. 2.** SEM images of Mg foil working electrodes after 30 continuous minutes of stripping in EtMgBr at (a) 500 mV, (b) 700 mV, and (c) 900 mV. Counter and reference electrodes were polished strips of Mg ribbon.
- **Fig. 3.** Electrochemical results from potentiostatic deposition/dissolution cycling of polished Mg foils in EtMgBr. (a) deposition/dissolution cycling data for 10 cycles (15 minutes per half cycle) at three different potentials: -/+ 300 mV (dash); -/+ 500 mV (solid); -/+ 700 mV (dash-dot). (b) A plot of the deposition/dissolution ratio presented as a percentage for -/+ 300 mV (square); -/+ 500 mV (circle); -/+ 700 mV (triangle). Counter and reference electrodes were polished strips of Mg ribbon.
- **Fig. 4.** SEM images of each Mg foil working electrode after the completion of the 10 cycles for each of the experiments presented in Fig. 3a; (a) -/+ 300 mV, (b) -/+ 500 mV, and (c) -/+ 700 mV.
- **Fig. 5.** Plots of the XPS results for polished Mg foils after different electrochemical processes: (*p*) polished, no electrochemistry, (*s*) stripped at +500 mV for 30 minutes in EtMgBr, and (*c*) 10 potentiostatic deposition/dissolution cycles at -/+ 500 mV (15 minutes per half cycle) in EtMgBr.

Plot of binding energies in the ranges of (a) Oxygen (1s), (b) Bromine (3d), and (c) Magnesium (2p) are presented. For electrochemical processes the counter and reference electrodes were polished strips of Mg ribbon.

Fig. 6. HIM images of Mg residual structures on the surface of polished Mg foil after 20 potentiostatic deposition/dissolution cycles (15 minutes per half cycle) at -/+ 500 mV. (a/c) Normal incidence view (b/d) cross-section view at 45 degrees in relation to (a/c) respectively. Counter and reference electrodes were polished strips of Mg ribbon.

Fig. 7. Illustrative representation of the proposed progression of the Mg surface morphology. (a) Initial stripping of the oxide layer (dark grey) leads to pitting into the substrate (light grey). (b) Deposition favors the relatively unpassivated Mg {0001} surface resulting in hexagonal crystals (orange) normal to the surface. (c) Anisotropic stripping occurs on the {0001} Mg plane of the crystal. (d) Subsequent deposition (blue) occurs within hexagonal structures forming elongated, nested residual structures.

Supporting Information figure captions

Fig. S1. Cyclic voltammogram of EtMgBr on a Mg foil working electrode. Cycles were ran at 10 mV s⁻¹ versus a reference electrode of polished Mg ribbon.

Fig. S2. Plot of charge density versus pit density with a linear fit forced through the origin (a). Calculations of the average pit diameter from (a) according to a hemispherical model fit within error of the measured pit diameter from SEM images (b). Results show a strong correlation of pit density, but not an increase in size of the pit with increasing potential applied.

Fig. S3. SEM image (a) and corresponding FFT magnitude spectrum (b) of a Mg foil sample held at 900 mV vs Mg for 1800s. The perpendicular nature of the stripping lines and FFT intensity is indicative of the parallel orientation yet varied spacing of the pits.

Fig. S4. X-ray characterization of preferred oriented (PO) and randomly oriented (RO) Mg substrates. (a) XRD 2-theta plot of the (PO) and (RO) orientations. X-ray pole figures of the (002) line of the preferred oriented (b) and the random oriented Mg substrates.

Fig. S5. Electrochemical results from the Galvanostatic cycling of Mg foil. (a) dissolution/deposition data for 10 cycles (15 minutes per half cycle) at +/- 0.15 mA cm⁻². (b) SEM image of Mg foil working electrode at normal incidence after the completion of the 10 cycles. Counter and reference electrodes were polished strips of Mg ribbon.

Fig. S6. Electrochemical results from the potentiostatic cycling of Mg foil starting at a stripping potential and ending at a deposition potential. (a) dissolution/deposition data for 10 cycles (15 minutes per half cycle) at +/- 500 mV. (b) SEM image of Mg foil working electrode at normal incidence after the completion of the 10 cycles. Counter and reference electrodes were polished strips of Mg ribbon.

Fig. S7. Electrochemical results from the potentiostatic cycling of a polished randomly oriented Mg substrate. (a) deposition/dissolution data for 10 cycles (15 minutes per half cycle) at -/+ 500 mV. (b) SEM image of the Mg substrate working electrode at normal incidence after the completion of the 10 cycles. Counter and reference electrodes were polished strips of Mg ribbon.

Fig. S8. SEM images of Mg columnar growth from the surface of polished Mg foil after 200 potentiostatic dissolution/deposition cycles (15 minutes per half cycle) at +/- 500 mV. (a) Isolated columns. (b) Zoomed-in image of one of the columns from (a), showing the striations on the side. Images were obtained at a 30 degree tilt. Counter and reference electrodes were polished strips of Mg ribbon.